Multigain Online Autotuning Technique-Based Discrete-Time Current Regulator for Permanent Magnet Synchronous Motors

Weiqiu Zhang, Zhuoran Zhang, *Senior Member, IEEE*, Liyan Wen, Weijia Jiang, *Student Member, IEEE*, Xiangpei Gu, and Yanhui Li

***Abstract*—In this article, a multigain online autotuning technique-based discrete-time current regulator for permanent magnet synchronous motors is proposed. With the nominal current regulator in the proposed control scheme, the performance and robustness of the current control system are improved. Then, a multigain online autotuning method is proposed to further suppress the adverse effects of parametric uncertainties. In the proposed approach, the voltage vectors of the current regulator are mapped to an extended synchronous reference frame, based on which an adaptive observer is constructed without approximation to autotune the gains of the current regulator online. Compared with traditional recursive least-squares methods, the proposed autotuning method can be implemented with greatly reduced computational burden. The proposed current control method is designed directly in the discrete-time domain, which guarantees the control performance in digital implementations. In addition, the proposed current control method can be applied to both the interior and surface-mounted permanent magnet synchronous motors. Finally, theoretical analysis and comparative experiments verify the effectiveness of the proposed method.**

***Index Terms*—Adaptive observer, current regulator, discrete-time domain, online autotuning technique, permanent magnet synchronous motor (PMSM).**

NOMENCLATURE

u_d, u_q	dq-axis voltages.
i_d, i_q	dq-axis currents.
$i_{d\text{ref}}, i_{q\text{ref}}$	Reference of dq-axis currents.
$R_s, \widehat{R}_s$	Stator resistor and its estimation.
$L_d, \widehat{L}_d$	d-axis stator inductance and its estimation.
$L_q, \widehat{L}_q$	q-axis stator inductance and its estimation.
ω_e	Motor electrical angular frequency.
φ_f	Flux linkage due to the permanent magnets.
n	Motor speed.
FEA	Finite-element analysis.

Manuscript received 4 February 2023; revised 27 June 2023; accepted 17 September 2023. Date of publication 2 October 2023; date of current version 6 December 2023. This work was supported in part by the National Natural Science Foundation of China under Grant U2141223 and in part by the Postgraduate Research & Practice Innovation Program of Jiangsu Province under Grant KYCX23_0376. Recommended for publication by Associate Editor H. Hofmann. *(Corresponding author: Zhuoran Zhang.)*

Weiqiu Zhang, Zhuoran Zhang, Weijia Jiang, Xiangpei Gu, and Yanhui Li are with Center for More-Electric-Aircraft Power System, Nanjing University of Aeronautics and Astronautics, Nanjing 211106, China (e-mail: zhangweiqiu@nuaa.edu.cn; apsc-zzr@nuaa.edu.cn; jiangweijia@nuaa.edu.cn; guxiangpei@nuaa.edu.cn; lyh_nuaa@nuaa.edu.cn).

Liyan Wen is with the Key Laboratory of Navigation, Control and Health-Management Technologies of Advanced Aerocraft, Ministry of Industry and Information Technology, Nanjing University of Aeronautics and Astronautics, Nanjing 211106, China (e-mail: wenliyan_2017@nuaa.edu.cn).

Color versions of one or more figures in this article are available at https://doi.org/10.1109/TPEL.2023.3321112.

Digital Object Identifier 10.1109/TPEL.2023.3321112

I. INTRODUCTION

THE permanent magnet synchronous motors (PMSMs) are used in aircraft electric propulsion, locomotive traction, and ship propulsion due to their high efficiency, power density, and torque density [1]. In these applications, the current control performance of the motors is critical. The modern control methods are usually implemented in digital processors, so the current regulator designed in the discrete-time domain can guarantee its performance in the digital implementation [2].

The discrete-time current regulators can be divided into two categories: proportional (P) control and proportional–integral (PI) control. In terms of the P control method, the typical method is the model-based method, such as the deadbeat [3], [4] and continuous-control-set model-predictive current regulator [5], while model-based current regulators are relatively more sensible to motor electrical parameters. The PI control method is a good alternative. In [6] and [7], the current regulator based on discrete-time pole-placement design is proposed. A novel structure for the digital internal model current controller is proposed in [8]. The improved effectiveness of these methods compared with continuous-time domain-designed methods is verified by experiments, while they are relatively complicated due to a complicated matrix exponential $e^{\mathbf{A}T_s}$ [9]. Then, in order to reduce complexity, the complex vector principle is introduced. The discrete-time complex vector PI current regulator for surface-mounted permanent magnet synchronous motors (SPMSMs) that also demonstrates improved response is proposed in [2]. The digital complex vector current regulator is expanded to interior permanent magnet synchronous motors (IPMSMs) through a flux model [9], [10].

However, motors in some applications are required for high speed, high power, and high power density. These motors are usually designed with more poles, higher tip speed, fewer series turns per phase, and even no iron core, which leads to very low resistance and inductance parameters. In [11], the design of a motor for electrical propulsion aviation is demonstrated. Its

resistance and inductance parameters are 16 mΩ and 9.25 μH, respectively. The resistance and inductance of a high-speed motor investigated in [3], which can be used in robot joints, industrial servo motors, and actuators, are only 45 mΩ and 24 μH, respectively. For these motors, the small parameter errors can still significantly deteriorate the response of the current regulator [12], even though the discrete-time current regulator provides higher robustness. The parameter identification method and the self-commissioning technique, which have been widely investigated to improve the performance of the motor drive system, are effective countermeasures [13], [14]. First of all, the direct calculation method like the method used in [4] is not considered, because this method makes the identified parameter greatly sensible to the disturbances like the sampling noise, which is also illustrated in [3]. Then, there are three main types of online estimation methods. The first method is the AI-based methods [15], [16]. However, these algorithms need to be executed on highly efficient hardware.

The second method is the numerical method, in which the recursive least-squares (RSL) method is widely studied. In [5] and [17], the RSL-based methods are used to estimate the resistance, inductance, torque, or flux linkage. While as illustrated in [3], RSL brings a heavy computing burden, the convergence in some applications cannot be guaranteed, and the RLS-associated methods may be difficult to be applied to the fully discretized model.

Finally, some observers, which can be implemented more simply, are utilized. In [18], [19], and [20], the sliding-mode observer is used to deal with inverter nonlinearity and system uncertainty, while the sliding-mode observer may lead to severe chattering and even instability [18]. In [21], [22], [23], and [24], the disturbance observer is utilized to suppress the external disturbance and uncertainty in the servo and drive systems, whereas it is difficult to extract the individual parameters from lumped disturbances [14]. Then, in [25] and [26], the adaptive observer is used to estimate the back electromotive force, speed, and position of motors in the sensorless motor drive. It is clear that the adaptive-observer-based methods have the disadvantage of complicated design processes [14]. However, compared with the disturbance observer, the adaptive observer can flexibly select the parameters that need to be adjusted by the adaptive law. The computational efficiency is greatly improved compared with RSL. Therefore, the adaptive observer becomes the choice of this article.

In this article, in order to reduce the complexity of the regulator, the complex vector principle is utilized, and a fully discretized double-vector model for the PMSM is derived instead of the flux model and the conventional complex vector model. This model retains the advantages of the conventional complex vector model, which is more accurate than the flux model and simpler than the state-space model. Meanwhile, it can be applied to both IPMSM and SPMSM like the flux model. Based on the model, a nominal discrete-time current regulator is developed. Its better regulation performance and higher robustness are verified by theoretical analysis and comparative experiments. However, the analysis and experiments indicate that small parameter errors still significantly deteriorate the current response when the resistance and the inductance parameters of the motors are low. Then, a multigain online autotuning method is proposed. In the proposed autotuning method, the adaptive observer is established in an extended synchronous reference frame. It has a clearer and more direct relationship between the observation errors and gains. To be more specific, an observed state quantity is associated with only one gain to be estimated. This is beneficial to simplifying the design approach and makes the approximation methods like Taylor expansion utilized in [3] not used. Meanwhile, compared with the extensively used RLS-based methods, the proposed method is based on the fully discretized model, and the computational burden is greatly reduced. Finally, the multigain online autotuning technique-based discrete-time current control scheme is constructed for PMSMs, and experiments are carried out to validate its effectiveness.

The rest of this article is organized as follows. In Section II, the discrete-time model is developed, and the useful lemmas are given. In Section III, the design approaches of the nominal current regulator are presented, and its robustness is analyzed. Then, the multigain online autotuning technique is motivated. In Section IV, the validation experiments are conducted. Finally, Section V concludes this article.

II. Preliminaries

In this section, the fully discretized double-vector model of the PMSM is developed. The useful lemmas are reviewed.

A. Discrete-Time Model of the PMSM

In the synchronous reference frame, the model of the PMSM in the continuous-time domain is given as

$$u_d = R_s i_d + L_d \frac{di_d}{dt} - \omega_e L_q i_q \tag{1}$$

$$u_q = R_s i_q + L_q \frac{di_q}{dt} + \omega_e L_d i_d + \omega_e \varphi_f. \tag{2}$$

Based on the complex vector principle, models (1) and (2) can be rewritten with two voltage vectors and two current vectors to derive the double-vector model as

$$\boldsymbol{u_{vd}} = (R_s + j\omega_e L_d)\boldsymbol{i_{vd}} + L_d \frac{d\boldsymbol{i_{vd}}}{dt} \tag{3}$$

$$\boldsymbol{u_{vq}} = (R_s + j\omega_e L_q)\boldsymbol{i_{vq}} + L_q \frac{d\boldsymbol{i_{vq}}}{dt} + j\omega_e \varphi_f \tag{4}$$

where $\boldsymbol{u_{vd}}$, $\boldsymbol{u_{vq}}$, $\boldsymbol{i_{vd}} = i_d + j0$ and $\boldsymbol{i_{vq}} = 0 + ji_q$ are the dq-axis voltage vectors and current vectors, respectively. Then, using the discretization method in [2], the models (3) and (4) can be discretized as

$$\boldsymbol{i_{vd}}(k+1) = \frac{e^{-\frac{R_s}{L_d}T_s}}{e^{j\omega_e T_s}}\boldsymbol{i_{vd}}(k) + \frac{1-e^{-\frac{R_s}{L_d}T_s}}{R_s e^{j\omega_e T_s}}\left(\frac{\boldsymbol{u_{vd}}(k-1)}{e^{j\omega_e T_s}} - \boldsymbol{E_{vd}}(k)\right) \tag{5}$$

$$\boldsymbol{i_{vq}}(k+1) = \frac{e^{-\frac{R_s}{L_q}T_s}}{e^{j\omega_e T_s}}\boldsymbol{i_{vq}}(k) + \frac{1-e^{-\frac{R_s}{L_q}T_s}}{R_s e^{j\omega_e T_s}}\left(\frac{\boldsymbol{u_{vq}}(k-1)}{e^{j\omega_e T_s}} - \boldsymbol{E_{vq}}(k)\right) \tag{6}$$

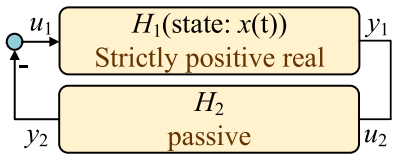

Fig. 1. Feedback connection in Lemma 2.1.

where

$$\boldsymbol{E_{vd}}(k) = -\frac{\omega_e(k)\varphi_f}{T_s}\int_0^{T_s}(\sin\omega_e(k)t)\,\mathrm{d}t = -\frac{\varphi_f}{T_s}(1-\cos\omega_e(k)T_s) \tag{7}$$

$$\boldsymbol{E_{vq}}(k) = j\frac{\omega_e(k)\varphi_f}{T_s}\int_0^{T_s}(\cos\omega_e(k)t)\,\mathrm{d}t = j\frac{\varphi_f}{T_s}\sin\omega_e(k)T_s \tag{8}$$

are the integral average of the back electromotive force.

Based on (5) and (6), the model of the PMSM in the discrete-time frequency domain is derived as

$$G_{vd}(z) = \frac{\boldsymbol{i_{vd}}(z)}{\boldsymbol{u_{vd}}(z)} = \frac{1}{zk_{dex}e^{j\omega_eT_s}-k_{dbl}}\cdot\frac{1}{ze^{j\omega_eT_s}} \tag{9}$$

$$G_{vq}(z) = \frac{\boldsymbol{i_{vq}}(z)}{\boldsymbol{u_{vq}}(z)} = \frac{1}{zk_{qex}e^{j\omega_eT_s}-k_{qbl}}\cdot\frac{1}{ze^{j\omega_eT_s}} \tag{10}$$

with

$$k_{dex} = \frac{R_s}{1-e^{-\frac{R_s}{L_d}T_s}},\quad k_{dbl} = e^{-\frac{R_s}{L_d}T_s}k_{dex} \tag{11}$$

$$k_{qex} = \frac{R_s}{1-e^{-\frac{R_s}{L_q}T_s}},\quad k_{qbl} = e^{-\frac{R_s}{L_q}T_s}k_{qex}. \tag{12}$$

B. Useful Theorem and Lemma

In order to design the multigain autotuning method from the stability analysis, the following lemmas are utilized.

Lemma 2.1 (Asymptotic hyperstability [27]): Consider the feedback connection of a linear time-invariant block H_1 (state: $x(t)$), which is characterized by a strictly positive real transfer function (see Fig. 1), with a block H_2 characterized by

$$\eta(0,t_1) \geqslant \sum_{t=0}^{t_1} y_2^T(t)u_2(t) \geqslant -\gamma_0^2, \gamma_0^2 < \infty \quad \forall t_1 > 0. \tag{13}$$

Then,

$$\lim_{t\to\infty}x(t) = 0; \lim_{t\to\infty}u_1(t) = \lim_{t\to\infty}y_1(t) = 0 \quad \forall x(0). \tag{14}$$

Definition 2.2 [28]: Let $H(z)$ be a square real rational transfer matrix in z. $H(z)$ is said to be strictly positive realness if it is analytic in $|z| \geqslant 1$ and

$$\mathbf{H}(e^{j\theta}) + \mathbf{H}^T(e^{-j\theta}) > 0 \qquad \forall\theta\in[0,2\pi]. \tag{15}$$

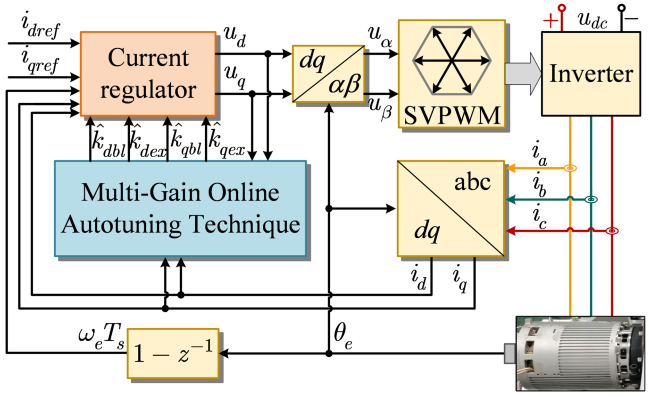

Fig. 2. Diagram of the proposed current control system.

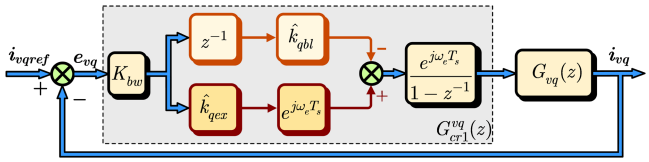

Fig. 3. Diagram of the q-axis current control system.

III. Discrete-Time Current Regulator Based on the Multigain Online Autotuning Technique

In this section, the analysis and design approaches of the proposed discrete-time current control method, as shown in Fig. 2, are presented.

A. Approaches of Nominal Current Regulator Design

Based on (9) and (10), the principle of pole-zero cancellation and internal model, the nominal discrete complex vector current regulator with the bandwidth factor K_{bw}, which is called CR1, is designed as

$$G_{cr1}^{vd}(z) = \frac{K_{\mathrm{bw}}(\hat{k}_{dex}e^{j\omega_eT_s}-z^{-1}\hat{k}_{dbl})}{1-z^{-1}}e^{j\omega_eT_s} \tag{16}$$

$$G_{cr1}^{vq}(z) = \frac{K_{\mathrm{bw}}(\hat{k}_{qex}e^{j\omega_eT_s}-z^{-1}\hat{k}_{qbl})}{1-z^{-1}}e^{j\omega_eT_s} \tag{17}$$

where $\hat{k}_{dex}$, $\hat{k}_{dbl}$, $\hat{k}_{qex}$, and $\hat{k}_{qbl}$ are the estimations of k_{dex}, k_{dbl}, k_{qex}, and k_{qbl}, respectively. The current closed-loop control system of the q-axis is shown in Fig. 3, where $\boldsymbol{i_{vq}}_{\mathrm{ref}} = 0 + ji_{\mathrm{qref}}$ and $\boldsymbol{e_{vq}} = \boldsymbol{i_{vq}}_{\mathrm{ref}} - \boldsymbol{i_{vq}}$ are the current reference vector and the error vector, respectively. The control system structure of d-axis with the reference vector $\boldsymbol{i_{vd}}_{\mathrm{ref}} = i_{\mathrm{dref}} + j0$ and the error vector $\boldsymbol{e_{vd}} = \boldsymbol{i_{vd}}_{\mathrm{ref}} - \boldsymbol{i_{vd}}$ is the same as that of the q-axis.

In the absence of parameter errors, the open-loop pulse transfer function is derived as

$$G_{n-op}^{vd}(z) = G_{cr1}^{vd}(z)G_{vd}(z) = \frac{K_{\mathrm{bw}}}{z^2-z} \tag{18}$$

$$G_{n-op}^{vq}(z) = G_{cr1}^{vq}(z)G_{vq}(z) = \frac{K_{\mathrm{bw}}}{z^2-z}. \tag{19}$$

Then, the parameter K_{bw} is tuned as 0.35 to make the performance of (18) and (19) meet the metrics as follows:

TABLE I
PARAMETERS OF THE CONTROL PLANT

Symbol	Parameter	Value
I_N	Rated current	150 A
n_N	Rated rotating speed	3000 r/min
n_p	Poles	20
φ_f	Flux linkage	0.15 mWb
R_s	Stator resistance (FEA)	2 mΩ
L_d	D-axis stator inductance (FEA)	8 μH
L_q	Q-axis Stator inductance (FEA)	8 μH
$U_{\rm dc}$	DC-link voltage	100 V
f_s	Switching frequency of the inverter	30 kHz

1) gain margin (GM): GM $\geq$ 6 dB;
2) phase margin (PM): 30° $\leq$ PM $\leq$ 60°;
3) modulus margin (MM): MM ≥ -6 dB;
4) delay margin (DM): DM $\geq T_s$.

B. Influence of the Parameter Errors

The theoretical analysis and experimental comparison in [9] has shown that the current regulator in [9] is more advanced than some other regulators. Therefore, CR1 is compared with the regulator in [9], which is represented by CR2. The adverse effects of parameter errors are analyzed. The parameters of the motor analyzed are shown in Table I.

From [9], the transformer function of CR2 is given as

$$G_{cr2}(z)=G_l\frac{k_{\rm bw}(e^{j\omega_eT_s}-z^{-1}e^{-\frac{\hat R_s}{\hat L_d}T_s})(\frac{\hat R_s}{\hat L_d}+j\omega_e)}{(e^{j\omega_eT_s}-e^{-\frac{\hat R_s}{\hat L_d}T_s})(1-z^{-1})}k_1 \quad (20)$$

with $k_{\rm bw}=0.35$ and

$$G_l={\rm diag}\left(\hat L_d,\hat L_q\right) \quad (21)$$

$$k_1=\frac{2}{\omega_eT_s}\sin(\frac{\omega_eT_s}{2})e^{j1.5\omega_eT_s}. \quad (22)$$

The analysis of the robustness to the parameter errors is based on the following open-loop transfer functions:

$$G^d_{opcr1}(z)=G_{vd}(z)G^{vd}_{cr1}(z) \quad (23)$$

$$G^q_{opcr1}(z)=G_{vq}(z)G^{vq}_{cr1}(z) \quad (24)$$

$$G^d_{opcr2}(z)=G_{vd}(z)G_{cr2}(z) \quad (25)$$

$$G^q_{opcr2}(z)=\frac{G_{vq}(z)G_{cr2}(z)}{1+k_1\hat R_sG_{vq}(z)\left(\hat L_q/\hat L_d-1\right)}. \quad (26)$$

Fig. 4 shows the range of estimated parameters used in CR1 and CR2 that can stabilize the current control system. The estimated parameters in the area shown in Fig. 4(a) can stabilize $G^d_{opcr1}(z)$ and $G^q_{opcr1}(z)$. The parameters in the area shown in Fig. 4(b) can stabilize $G^d_{opcr2}(z)$ and $G^q_{opcr2}(z)$. The wider range of CR1 indicates the higher robustness of CR1.

Then, to more intuitively reflect the adverse effects of parameter errors, the simulation is carried out with the cases as follows under the condition of $n=3000$ r/min and stepping $i_{q\rm ref}=150$ A. The motor parameters are set according to Table I.

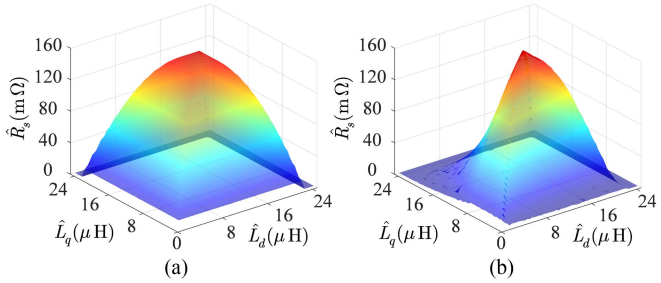

Fig. 4. Range of the parameter estimations that can stabilize the current control system with different regulators: (a) CR1 and (b) CR2.

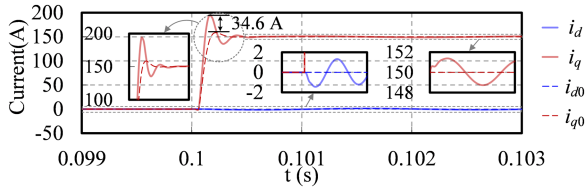

Fig. 5. Performance of CR1 with cases 1 and 2.

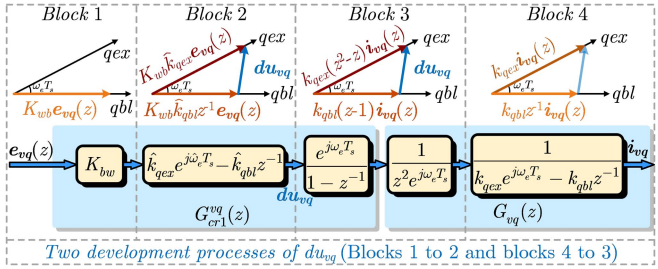

Fig. 6. Development process of $\boldsymbol{du_{vq}}$ in the q-axis current control system.

1) Case 1: $\hat R_s=R_s$, $\hat L_d=L_d$, and $\hat L_q=L_q$. The dq-axis currents are recorded as i_{d0} and i_{q0}.
2) Case 2: $\hat R_s=0.5R_s$, $\hat L_d=1.5L_d$, and $\hat L_q=1.5L_q$. The dq-axis currents are recorded as i_d and i_q.

The resistance and inductance parameter errors in case 2 are only 1 mΩ, 4 μH, and 4 μH, respectively. According to the simulation results shown in Fig. 5, it is clear that the overshoot of i_q increases by 34.6 A, and the dq-axis current oscillations are aggravated.

In conclusion, even though the regulator CR1 is relatively more robust, the small parameter errors still have a significant deterioration effect on the current control system of the motors with small resistance and inductance parameters.

C. Adaptive-Observer-Based Multigain Online Autotuning Technique

As shown in Fig. 6, the q-axis is extended to the qex-axis and the qbl-axis. The voltage vector $\boldsymbol{du_{vq}}$ is decomposed into components on the qex-axis and the qbl-axis. Blocks 1 and 2 illustrate the development process from the error vector $\boldsymbol{e_{vq}}$ to the voltage vector $\boldsymbol{du_{vq}}$. Blocks 3 and 4 illustrate the development process from the current vector $\boldsymbol{i_{vq}}$ to the voltage vector $\boldsymbol{du_{vq}}$. The process of the d-axisis the same as that of the q-axis.

Then, the two composition methods of $\boldsymbol{du_{vd}}$ or $\boldsymbol{du_{vq}}$ in blocks 2 and 3 indicate the following equation:

$$\mathbf{U}(z) = \mathbf{K}(z)\mathbf{I}(z) \tag{27}$$

with

$$\mathbf{U}(z) = \begin{bmatrix} K_{\text{bw}}\widehat{k}_{dex}z^{-2}e_d(z) \\ K_{\text{bw}}\widehat{k}_{dbl}z^{-3}e_d(z) \\ K_{\text{bw}}\widehat{k}_{qex}z^{-2}e_q(z) \\ K_{\text{bw}}\widehat{k}_{qbl}z^{-3}e_q(z) \end{bmatrix} \tag{28}$$

$$\mathbf{I}(z) = \begin{bmatrix} (1-z^{-1})i_d(z) \\ (z^{-1}-z^{-2})i_d(z) \\ (1-z^{-1})i_q(z) \\ (z^{-1}-z^{-2})i_q(z) \end{bmatrix} \tag{29}$$

$$\mathbf{K} = \text{diag}(k_{dex}, k_{dbl}, k_{qex}, k_{qbl}). \tag{30}$$

Then, the gain-adaptive observer is designed as

$$\widehat{\mathbf{U}}(z) = \widehat{\mathbf{K}}(z)\mathbf{I}(z) \tag{31}$$

where $\widehat{\mathbf{K}}(z) = \mathcal{L}[\widetilde{\mathbf{U}}(z), \mathbf{I}(z)]$ is the adaptive gain matrix tuned by the adaptive law $\mathcal{L}[\widetilde{\mathbf{U}}(z), \mathbf{I}(z)]$, $\widehat{\mathbf{U}}(z) = \widehat{\mathbf{K}}\mathbf{I}(z)$ is the observed voltage vector, and $\widetilde{\mathbf{U}}(z) = [\widetilde{u}_{dex}(z), \widetilde{u}_{dbl}(z), \widetilde{u}_{qex}(z), \widetilde{u}_{qbl}(z)]^T = \mathbf{U}(z) - \widehat{\mathbf{U}}(z)$ is the error voltage vector.

The adaptive law $\mathcal{L}[\widetilde{\mathbf{U}}(z), \mathbf{I}(z)]$ can be designed as follows.

Step 1: The nonlinear negative feedback system shown in Fig. 1 is established as

$$y_1 = u_2 = \widetilde{\mathbf{U}}(z), y_2 = -u_1 = \mathbf{V}(z) = H_2\widetilde{\mathbf{U}}(z) \tag{32}$$

$$H_1 = \mathbf{G}_{\text{fwd}}(z) = (\mathbf{J} - z^{-1}\mathbf{A})^{-1} \tag{33}$$

where $\mathbf{A} = \text{diag}(\alpha_{dex}, \alpha_{dbl}, \alpha_{qex}, \alpha_{qbl})$ and $\mathbf{J}$ is the identity matrix. H_2 is designed in step 3.

Step 2: The coefficient matrix $\mathbf{A}$ is determined to make the forward path strictly positive real. According to definition 2.2, applying the lemma to $\mathbf{G}_{\text{fwd}}(z)$ yields the following inequality:

$$\begin{aligned} &\mathbf{G}_{\text{fwd}}(e^{j\theta}) + \mathbf{G}_{\text{fwd}}(-e^{j\theta}) \\ &= \text{diag}\left(\begin{matrix} 1 + \frac{1-\alpha_{dex}^2}{1-2\alpha_{dex}\cos\theta+\alpha_{dex}^2}, 1 + \frac{1-\alpha_{dbl}^2}{1-2\alpha_{dbl}\cos\theta+\alpha_{dbl}^2}, \\ 1 + \frac{1-\alpha_{qex}^2}{1-2\alpha_{qex}\cos\theta+\alpha_{qex}^2}, 1 + \frac{1-\alpha_{qbl}^2}{1-2\alpha_{qbl}\cos\theta+\alpha_{qbl}^2} \end{matrix} \right) \\ &> 0. \end{aligned} \tag{34}$$

Then, the range of the parameters α_{dex}, α_{dbl}, α_{dex}, and α_{dbl} in the gain matrix is solved as

$$\alpha_{dex}, \alpha_{dbl}, \alpha_{qex}, \alpha_{qbl} \in (0, 1). \tag{35}$$

Step 3: According to Lemma 2.1, the adaptive law is designed by solving the following inequality:

$$\eta(0, k_1) \geqslant \sum_{k=0}^{k_1}(-\mathbf{V}^T(k)\widetilde{\mathbf{U}}(k)) \geqslant -\gamma_0^2, \gamma_0^2 < \infty \quad \forall k_1 > 0. \tag{36}$$

Then, (36) can be expanded into four functions as

$$\eta_{dex}(0, k_1) = \sum_{k=0}^{k_1} x_{dex}(k)(\hat{k}_{dex} - k_{dex}) \tag{37}$$

$$\eta_{dbl}(0, k_1) = \sum_{k=0}^{k_1} x_{dbl}(k)(\hat{k}_{dbl} - k_{dbl}) \tag{38}$$

$$\eta_{qex}(0, k_1) = \sum_{k=0}^{k_1} x_{qex}(k)(\hat{k}_{qex} - k_{qex}) \tag{39}$$

$$\eta_{qbl}(0, k_1) = \sum_{k=0}^{k_1} x_{qbl}(k)(\hat{k}_{qbl} - k_{qbl}) \tag{40}$$

with

$$\begin{aligned} x_{dex}(k) &= \widetilde{u}_{dex}(k)(i_d(k) - i_d(k-1)) \\ &\quad - \alpha_{dex}\widetilde{u}_{dex}(k)(i_d(k-1) - i_d(k-2)) \end{aligned} \tag{41}$$

$$\begin{aligned} x_{dbl}(k) &= \widetilde{u}_{dbl}(k)(i_d(k-1) - i_d(k-2)) \\ &\quad - \alpha_{dbl}\widetilde{u}_{dbl}(k)(i_d(k-2) - i_d(k-3)) \end{aligned} \tag{42}$$

$$\begin{aligned} x_{qex}(k) &= \widetilde{u}_{qex}(k)(i_q(k) - i_q(k-1)) \\ &\quad - \alpha_{qex}\widetilde{u}_{qex}(k)(i_q(k-1) - i_q(k-2)) \end{aligned} \tag{43}$$

$$\begin{aligned} x_{qbl}(k) &= \widetilde{u}_{qbl}(k)(i_q(k-1) - i_q(k-2)) \\ &\quad - \alpha_{qbl}\widetilde{u}_{qbl}(k)(i_q(k-2) - i_q(k-3)). \end{aligned} \tag{44}$$

Finally, the adaptive law is designed as

$$\hat{k}_{dex} = \sum_{i=0}^{k} a_{dex}x_{dex}(i) + b_{dex}x_{dex}(k) + k_{dex0} \tag{45}$$

$$\hat{k}_{dbl} = \sum_{i=0}^{k} a_{dbl}x_{dbl}(i) + b_{dbl}x_{dbl}(k) + k_{dbl0} \tag{46}$$

$$\hat{k}_{qex} = \sum_{i=0}^{k} a_{qex}x_{qex}(i) + b_{qex}x_{qex}(k) + k_{qex0} \tag{47}$$

$$\hat{k}_{qbl} = \sum_{i=0}^{k} a_{qbl}x_{qbl}(i) + b_{qbl}x_{qbl}(k) + k_{qbl0} \tag{48}$$

with

$$a_{dex}, a_{dbl}, a_{qex}, a_{qbl} > 0 \tag{49}$$

$$b_{dex} > -0.5a_{dex} \tag{50}$$

$$b_{qex} > -0.5a_{qex} \tag{51}$$

$$b_{dbl} > -0.5a_{dbl} \tag{52}$$

$$b_{qbl} > -0.5a_{qbl}. \tag{53}$$

Then, (36) holds as

$$\eta_{dex}(0, k_1) \geqslant -\frac{(k_{dex0}+k_{dex})^2}{2} \tag{54}$$

$$\eta_{dbl}(0, k_1) \geqslant -\frac{(k_{dbl0}+k_{dbl})^2}{2} \tag{55}$$

$$\eta_{qex}(0, k_1) \geqslant -\frac{(k_{qex0}+k_{qex})^2}{2} \tag{56}$$

$$\eta_{qbl}(0, k_1) \geqslant -\frac{(k_{qbl0}+k_{qbl})^2}{2}. \tag{57}$$

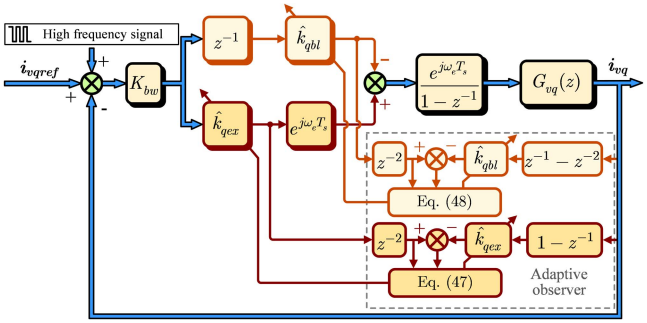

Fig. 7. Diagram of the q-axis current control system supported by the multigain online autotuning technique.

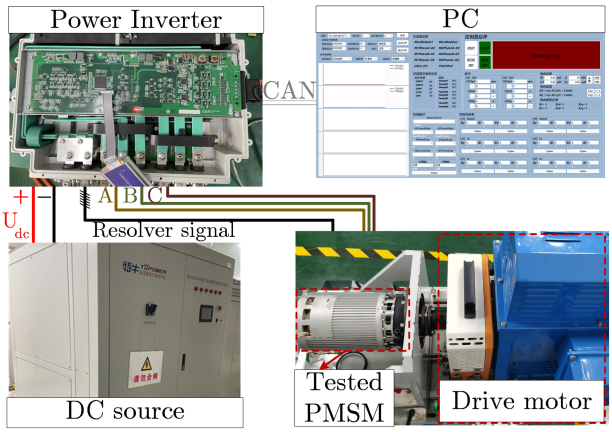

Fig. 8. Schematic diagram of the experimental platform.

Step 4: As shown in Fig. 7, a multigain online autotuning technique-based discrete-time current control scheme of the q-axis is constructed, which is represented as CR3. The control system of the d-axis is the same as that of the q-axis. In order to autotune the gains simultaneously and continuously, a high-frequency square signal is injected.

IV. Experimental Results

In this section, the experiments are carried out to verify the effectiveness of the proposed scheme. The motor drive platform is shown in Fig. 8. The parameters of the tested PMSM are shown in Table I. The digital processor is TMS320F28335. The program is saved in the flash of TMS320F28335, while it is executed in RAM by placing the control algorithm in the section "ramfuncs," based on which the execution time of different control methods is compared. The inverter adopts a three-phase two-level topology. During the experiment, the tested motor runs in the current control mode. The drive motor connected to the tested motor runs in the speed control mode and maintains the constant speed of the tested motor. In experiments, overshoot and ripple of i_q, as well as deviation extremum relative to 0 A and ripple of i_d, are discussed. All the experimental results are compared with the ideal q-axis step current response of $G_{cl}(z) = \frac{G^{vq}_{n-op}(z)}{1+G^{vq}_{n-op}(z)} = \frac{0.35}{z^2-z+0.35}$, which is recorded as i_{qn}, and the ideal d-axis decoupled current response, which is recorded as $i_{dn} = 0$ A. dq-axis currents regulated by CR1, CR2, and CR3 are recorded by i_{d1} and i_{q1}, i_{d2} and i_{q2}, and i_{d3} and i_{q3}, respectively.

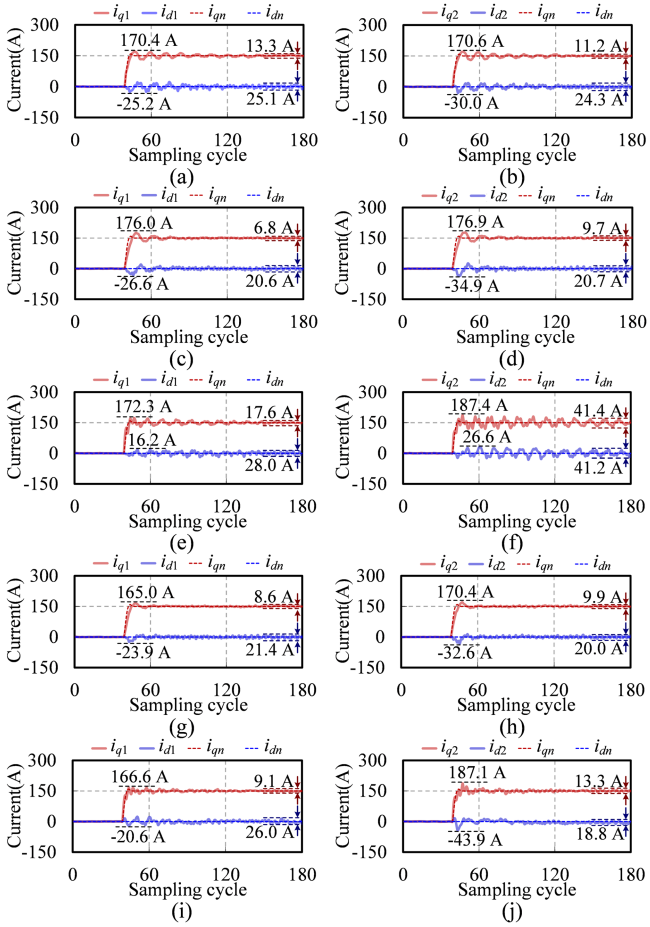

Fig. 9. Current performance of CR1 and CR2 with different cases. (a) CR1 with case 1. (b) CR2 with case 1. (c) CR1 with case 2. (d) CR2 with case 2. (e) CR1 with case 3. (f) CR2 with case 3. (g) CR1 with case 4. (h) CR2 with case 4. (i) CR1 with case 5. (j) CR2 with case 5.

A. Control Performance of the Nominal Current Regulator

In this experiment, CR1 is compared with CR2, and the adverse effect of parameter errors is also presented. The experimental results of the cases as follows under the condition of $n = 3000$ r/min and stepping i_{qref} from 0 to 150 A are presented in Figs. 9 and 10.

1) Case 1: $\hat{R}_s = R_s$, $\hat{L}_d = L_d$, and $\hat{L}_q = L_q$.
2) Case 2: $\hat{R}_s = 0.5R_s$, $\hat{L}_d = 0.5L_d$, and $\hat{L}_q = 0.5L_q$.
3) Case 3: $\hat{R}_s = 0.5R_s$, $\hat{L}_d = 1.5L_d$, and $\hat{L}_q = 1.5L_q$.
4) Case 4: $\hat{R}_s = 1.5R_s$, $\hat{L}_d = 0.5L_d$, and $\hat{L}_q = 0.5L_q$.
5) Case 5: $\hat{R}_s = 1.5R_s$, $\hat{L}_d = 1.5L_d$, and $\hat{L}_q = 1.5L_q$.

According to Figs. 9(a)–(d), (g), and (h) and 10, there is relatively small difference between CR1 and CR2 in cases 1, 2, and 4. However, the performance of CR1 changes less in different cases, especially the current ripple and the overshoot of i_q, which validates the stronger robustness of CR1. The gap between CR1 and CR2 is significant in cases 3 and 5.

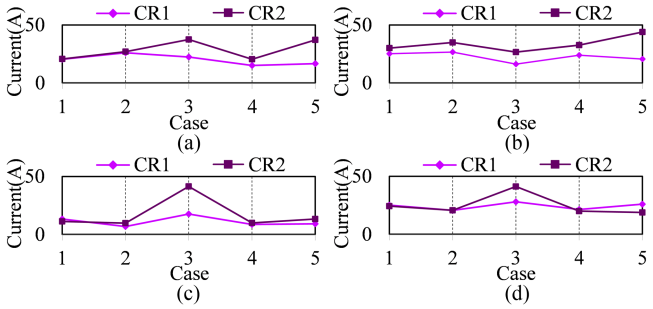

Fig. 10. Statistical comparisons of absolute values of different indexes with cases 1–5 in Section IV-A. (a) Overshoot of i_q. (b) Deviation extremum of i_d relative to 0 A. (c) q-axis current ripple. (d) d-axis current ripple.

According to Fig. 9(e) and (f), in case 3, the overshoot of i_q and deviation extremum of i_d regulated by CR1 are 22.3 and 16.2 A, respectively, while 37.4 and 26.6 A regulated by CR2. In the presented sampling cycles, the current has not fully converged. The d-axis current ripple regulated by CR2 is 13.2 A more than that regulated by CR1. The ripple of i_q is over two times higher than that regulated by CR1.

Similarly, in case 5, the gap is still significant, as shown in Fig. 9(i) and (j). The overshoot of i_q and deviation extremum of i_d regulated by CR2 are all over two times higher than that regulated by CR1.

It is noticeable that as implemented in case 1, the simulated or measured resistance and inductance parameters are usually used to design the regulator, while the experimental results indicate that the current response of the current control system in case 1 is greatly different from the ideal current response.

B. Validation of the Multigain Online Autotuning Technique

In order to verify the performance of the multigain online autotuning method under different speeds and current dynamics, the experiment with the following cases is carried out with tuned gains not updated to the regulator. Equations (11) and (12) show that the estimations of resistance and d-axis inductance parameters can be derived from $\widehat{k}_{dex}$ and $\widehat{k}_{dbl}$, and the estimations of resistance and q-axis inductance parameters can be derived from $\widehat{k}_{qex}$ and $\widehat{k}_{qbl}$. Therefore, the estimated parameters $\hat{R}_{sd}$ and $\hat{L}_d$ derived from $\widehat{k}_{dex}$ and $\widehat{k}_{dbl}$, as well as $\hat{R}_{sq}$ and $\hat{L}_q$ derived from $\widehat{k}_{qex}$ and $\widehat{k}_{qbl}$, are presented in Fig. 11(c)–(f).

1) Case 1: $n = 1500$ r/min, and $i_{q\text{ref}}$ is increased from 0 to 150 A in steps of 50 A.
2) Case 2: $n = 3000$ r/min, and $i_{q\text{ref}}$ is increased from 0 to 150 A in steps of 50 A.

Overall, the multigain online autotuning technique can make the four gains reach the steady state under different currents and speeds, which verifies the effectiveness of the autotuning method at the current dynamics and different speeds.

According to Fig. 11, when $i_{q\text{ref}}$ steps from 0 to 50 A, the autotuned gains and related resistance and inductance estimations vary greatly. It is probably because that inverter nonlinearity has a significant impact when the current control system is unloaded.

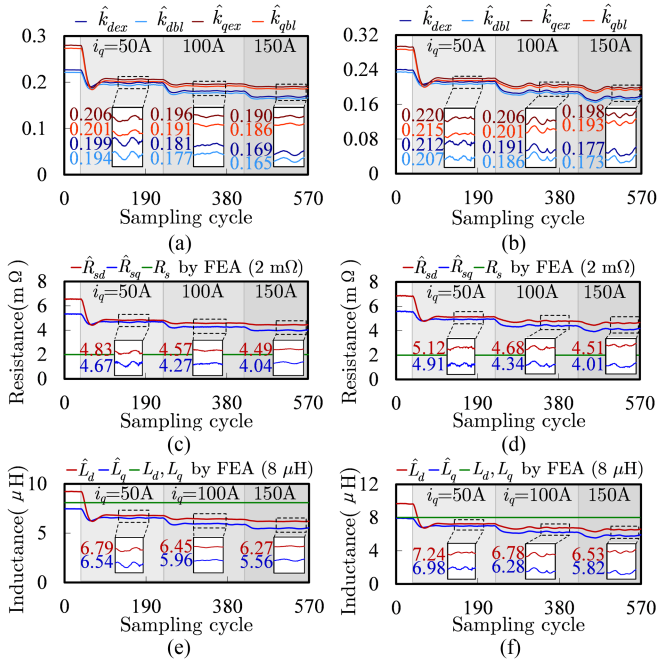

Fig. 11. Experimental results of the multigain online autotuning technique with different cases. The autotuned gains with (a) case 1 and (b) case 2. The resistance estimations with (c) case 1 and (d) case 2. The inductance estimations with (e) case 1 and (f) case 2.

Then, it is logical that as the current rises, the effect of the inverter nonlinearity is reduced. According to Fig. 11(a) and (b), with $i_{q\text{ref}}$ stepping from 100 to 150 A, the decreases of the four autotuned gains are only 0.006, 0.005, 0.012, and 0.012 in case 1, as well as 0.008, 0.008, 0.014, and 0.013 in case 2. Then, Fig. 11(c)–(f) indicates that compared with FEA, the deviation of estimated resistance and inductance parameters are less than 3.12 mΩ and 2.44 μH, respectively, while the accuracy will be investigated in Section IV-C by experiments.

C. Performance of the Multigain Online Autotuning Technique-Based Current Regulator

To validate the control performance of the current control system supported by the multigain online autotuning technique, the experiment is carried out with tuned gains updated to the regulator in the cases as follows. The results are presented in Fig. 12.

1) Case 1: $n = 1500$ r/min, and stepping $i_{q\text{ref}} = 150$ A.
2) Case 2: $n = 3000$ r/min, and stepping $i_{q\text{ref}} = 150$ A.

Overall, CR3 improves the dynamic performance of the current control system. According to the experimental results, the convergence values of the gains, resistance, and inductance parameters are, respectively, comparable at different speeds while different at different loads. Therefore, the autotuning method can run after the load changes and stop after the observed parameters converge, which can be easily implemented.

According to Fig. 12(a)–(c), the overshoot of i_q and the deviation extremum of i_d decrease by 4.5 and 6.6 A, respectively. The current oscillation is suppressed. During the dynamic state, the current response of i_q regulated by CR3 is more consistent

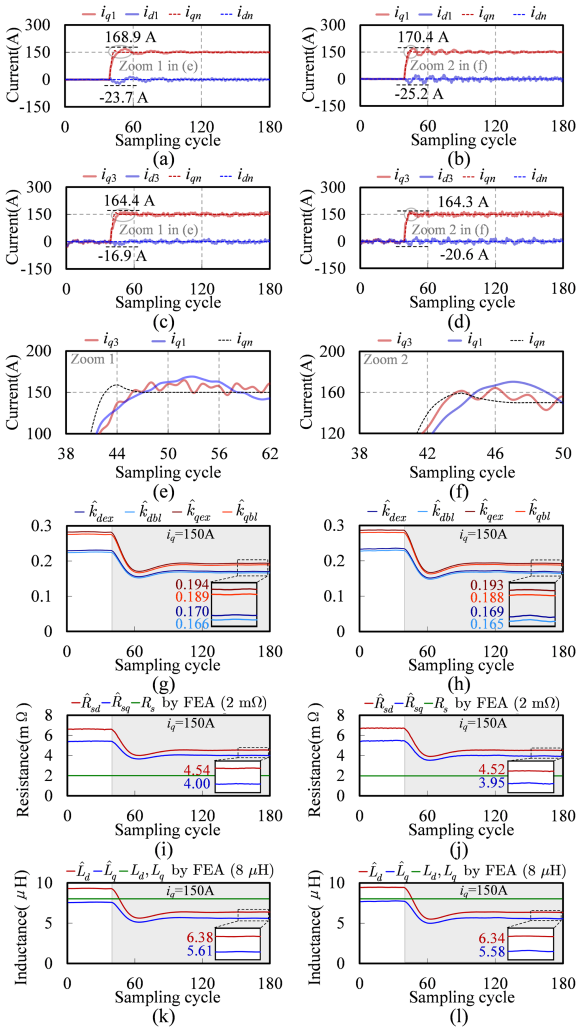

Fig. 12. Experimental results of CR1 and CR3 with different cases. dq-axis current regulated by CR1 with (a) case 1 and (b) case 2. dq-axis current regulated by CR3 with (c) case 1 and (d) case 2. (e) The zoom 1 of current waveform with case 1. (f) The zoom 2 of current waveform with case 2. The autotuned gains with (g) case 1 and (h) case 2. The resistance estimations with (i) case 1 and (j) case 2. The inductance estimations with (k) case 1 and (l) case 2.

with the ideal current response, which can be more clearly seen in Fig. 12(e).

Then, the improvement of autotuning technology on the current control system is more significant in case 2. According to Fig. 12(b) and (d), the overshoot of i_q and the deviation extremum of i_d decrease by 6.1 and 4.6 A, respectively. The current oscillation is also suppressed. With the regulation of CR3, the q-axis current with a faster rise rate and lower overshoot is also more consistent with the ideal current response, which can be more clearly seen in Fig. 12(l).

The improved current control performance indicates that the autotuned gains are more accurate, and the inconsistent dq-axis resistance and inductance parameters shown in Fig. 12(i)–(l) indicate the possible asymmetry of three-phase resistance and inductance parameters.

According to Fig. 12(a)–(d), the steady-state current ripple is increased due to high-frequency voltage injection. However, the

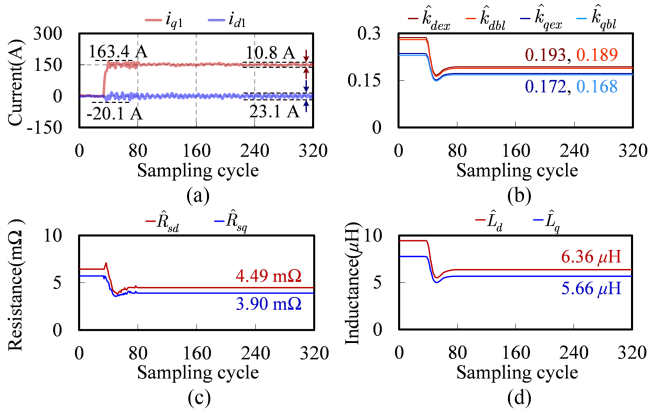

Fig. 13. Experimental results of CR3 with the autotuning method running all the time. (a) dq-axis current. (b) Autotuned gains. (c) Resistance estimations. (d) Inductance estimations.

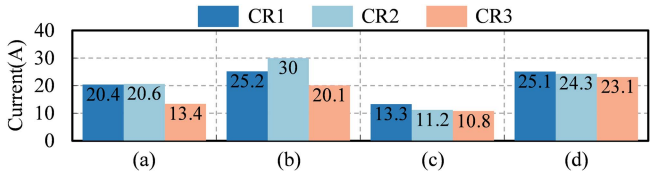

Fig. 14. Statistical comparison of CR1, CR2, and CR3. (a) Overshoot of i_q. (b) Deviation extremum of i_d relative to 0 A. (c) q-axis current ripple. (d) d-axis current ripple.

autotuning method does not need to run all the time. Thus, the experiment is conducted in case 2, where the autotuning method runs from the motor current change until the control parameters converge. As shown in Fig. 13, with the autotuning method, the control parameters, resistance parameter estimations, and inductance parameter estimations all converge after the change of i_q. The dynamic response of dq-axis current is still improved. Compared with the current response regulated by CR1 shown in Fig. 9(b), the overshoot of i_q and the deviation extremum of i_d decrease by 7 and 5.1 A, respectively, as shown in Fig. 9(b). Besides, the ripple of the dq-axis steady-state current is reduced by 2 and 2.5 A.

Finally, the control performance of CR1, CR2, and CR3 is compared in Fig. 14, which indicates the significant enhancement of the current control system by CR3, particularly in terms of dynamic performance.

D. Comparison With the Existing Parameter Estimation Methods

First, the proposal in this article is compared with the discrete-time parameter estimation method in [3], where some approximations are used to establish a clearer relationship between the estimated and actual parameters. As the method requires the injection of bias currents, which is different from the injection method in this article, the control parameters are first estimated, and then, the estimated parameters are used for the comparison of the current regulator performance. The current regulator with the estimated parameters by the proposal in this article is represented

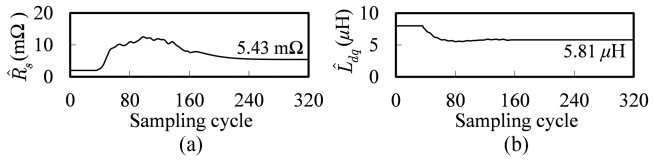

Fig. 15. Comparison of resistance and inductance parameters by the method in [3]. (a) Estimation of resistance parameter. (b) Estimation of inductance parameter.

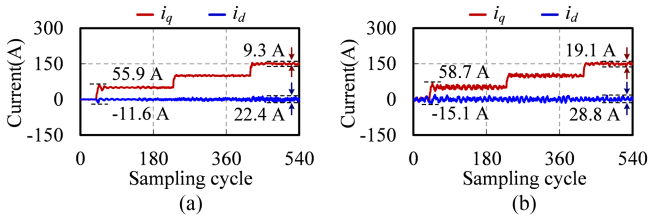

Fig. 16. Control performance of the current regulator with different gains. (a) CR4. (b) CR5.

TABLE II
COMPUTATIONAL BURDEN COMPARISON

	Method	Execution time
Regulator	Proposed Regulator	0.9 μs
	Regulator in [9]	2.3 μs
Autotuning Method	Proposed Method	0.8 μs
	Method in [3] (Identify one-axis parameters)	0.313 μs
	Conventional RLS Method	3 μs

by CR4, and the current regulator with the estimated parameters by the method in [3] is represented by CR5.

As shown in Fig. 15, the resistance and inductance parameters are, respectively, estimated by the method in [3]. The control gains $\hat{k}_{dex}$, $\hat{k}_{dbl}$, $\hat{k}_{qex}$, and $\hat{k}_{qbl}$ are derived as 0.177, 0.172, 0.177, and 0.172, respectively.

Then, the experiment is conducted at $n = 3000$ r/min and $i_{q\text{ref}} = 150$ A in steps of 50 A. The control performance of the current regulator is demonstrated in Fig. 16. According to the experimental results, when $i_{q\text{ref}} = 50$ A is applied, the deviation of i_d regulated by CR5 is -15.1 A, while it is -11.6 A regulated by CR4. The overshoot of i_q is 8.7 A regulated by CR5, while it is 5.9 A regulated by CR4. In addition, the ripples of the dq-axis current regulated by CR4 are 22.4 and 9.3 A, respectively, while they are 28.8 and 19.1 A regulated by CR5. Thus, the better control performance indicates the higher accuracy of the gains and parameters estimated by the method in this article.

The computational burden is compared as shown in Table II, where the discrete model based on the Euler difference method, which is simpler but less accurate, has been used to reduce the computational burden of the RLS method, while the execution time is still longer. Therefore, the reduced execution time validates the reduced complexity of the proposed scheme.

V. CONCLUSION

In this article, a multigain online autotuning technique-based discrete-time current regulator for PMSMs was proposed. The nominal current regulator in the current control scheme was proven to have better performance and higher robustness to parametric uncertainties, while it was difficult to obtain the accurate resistance and inductance parameters in practical applications. If the resistance and inductance parameters of the motor are very low, small parametric uncertainties still significantly deteriorate the performance of the current control system, which was presented in the theoretical analysis and experiments. The proposed multigain online autotuning method based on an adaptive observer can estimate the control gains more accurately and then significantly suppress the adverse effects of parameter errors. The proposed control method ran more efficiently, which was validated by the reduced execution time. In addition, the proposed current control method was designed directly in the discrete-time domain, which enabled the proposed control scheme to be directly implemented digitally without the unexpected deterioration of control performance or even instability of the current control system. The proposed current control method can be applied to both the IPMSM and the SPMSM. Finally, theoretical analysis and experimental comparison verify the effectiveness of the proposed method.

REFERENCES

[1] X. Zhang, C. L. Bowman, T. C. O'Connell, and K. S. Haran, "Large electric machines for aircraft electric propulsion," *IET Electr. Power Appl.*, vol. 12, no. 6, pp. 767–779, 2018.
[2] H. Kim, M. W. Degner, J. M. Guerrero, F. Briz, and R. D. Lorenz, "Discrete-time current regulator design for AC machine drives," *IEEE Trans. Ind. Appl.*, vol. 46, no. 4, pp. 1425–1435, Jul./Aug. 2010.
[3] Y. Yao, Y. Huang, F. Peng, J. Dong, and H. Zhang, "An improved deadbeat predictive current control with online parameter identification for surface-mounted PMSMs," *IEEE Trans. Ind. Electron.*, vol. 67, no. 12, pp. 10145–10155, Dec. 2020.
[4] S. Dai, J. Wang, Z. Sun, and E. Chong, "Transient performance improvement of deadbeat predictive current control of high-speed surface-mounted PMSM drives by online inductance identification," *IEEE Trans. Ind. Electron.*, vol. 69, no. 12, pp. 12358–12368, Dec. 2022.
[5] A. Brosch, O. Wallscheid, and J. Blöcker, "Torque and inductances estimation for finite model predictive control of highly utilized permanent magnet synchronous motors," *IEEE Trans. Ind. Inform.*, vol. 17, no. 12, pp. 8080–8091, Dec. 2021.
[6] N. Hoffmann, F. W. Fuchs, M. P. Kazmierkowski, and D. Schröder, "Digital current control in a rotating reference frame—Part I: System modeling and the discrete time-domain current controller with improved decoupling capabilities," *IEEE Trans. Power Electron.*, vol. 31, no. 7, pp. 5290–5305, Jul. 2016.
[7] M. Hinkkanen, H. A. A. Awan, Z. Qu, T. Tuovinen, and F. Briz, "Current control for synchronous motor drives: Direct discrete-time pole-placement design," *IEEE Trans. Ind. Appl.*, vol. 52, no. 2, pp. 1530–1541, Mar./Apr. 2016.
[8] I. Z. Petric, S. N. Vukosavic, M. Degano, and A. Galassini, "A digital internal model current controller for salient machines," *IEEE Trans. Ind. Electron.*, vol. 68, no. 6, pp. 4703–4717, Jun. 2021.
[9] X. Yuan, J. Chen, C. Jiang, and C. H. T. Lee, "Discrete-time current regulator for AC machine drives," *IEEE Trans. Power Electron.*, vol. 37, no. 5, pp. 5847–5858, May 2022.
[10] A. Altomare, A. Guagnano, F. Cupertino, and D. Naso, "Discrete-time control of high-speed salient machines," *IEEE Trans. Ind. Appl.*, vol. 52, no. 1, pp. 293–301, Jan./Feb. 2016.
[11] T. Balachandran, S. Srimmana, A. Anderson, X. Yi, N. Renner, and K. S. Haran, "Assembly and qualification of a slotless stator assembly for a MW-class permanent magnet synchronous machine," in *Proc. AIAA/IEEE Electr. Aircr. Technol. Symp.*, 2020, pp. 1–10.

[12] J. Yang, W.-H. Chen, S. Li, L. Guo, and Y. Yan, "Disturbance/uncertainty estimation and attenuation techniques in PMSM drives-a survey," *IEEE Trans. Ind. Electron.*, vol. 64, no. 4, pp. 3273–3285, Apr. 2017.
[13] S. A. Odhano, P. Pescetto, H. A. A. Awan, M. Hinkkanen, G. Pellegrino, and R. Bojoi, "Parameter identification and self-commissioning in AC motor drives: A technology status review," *IEEE Trans. Power Electron.*, vol. 34, no. 4, pp. 3603–3614, Apr. 2019.
[14] M. S. Rafaq and J.-W. Jung, "A comprehensive review of state-of-the-art parameter estimation techniques for permanent magnet synchronous motors in wide speed range," *IEEE Trans. Ind. Inform.*, vol. 16, no. 7, pp. 4747–4758, Jul. 2020.
[15] Z.-H. Liu, X.-H. Li, L.-H. Wu, S.-W. Zhou, and K. Liu, "GPU-accelerated parallel coevolutionary algorithm for parameters identification and temperature monitoring in permanent magnet synchronous machines," *IEEE Trans. Ind. Inform.*, vol. 11, no. 5, pp. 1220–1230, Oct. 2015.
[16] F.-J. Lin, S.-G. Chen, S. Li, H.-T. Chou, and J.-R. Lin, "Online autotuning technique for IPMSM servo drive by intelligent identification of moment of inertia," *IEEE Trans. Ind. Inform.*, vol. 16, no. 12, pp. 7579–7590, Dec. 2020.
[17] Y. Yu et al., "Full parameter estimation for permanent magnet synchronous motors," *IEEE Trans. Ind. Electron.*, vol. 69, no. 5, pp. 4376–4386, May 2022.
[18] D. Liang, J. Li, R. Qu, and W. Kong, "Adaptive second-order sliding-mode observer for PMSM sensorless control considering VSI nonlinearity," *IEEE Trans. Power Electron.*, vol. 33, no. 10, pp. 8994–9004, Oct. 2018.
[19] E.-K. Kim, J. Kim, H. T. Nguyen, H. H. Choi, and J.-W. Jung, "Compensation of parameter uncertainty using an adaptive sliding mode control strategy for an interior permanent magnet synchronous motor drive," *IEEE Access*, vol. 7, pp. 11913–11923, 2019.
[20] P. Mani, R. Rajan, L. Shanmugam, and Y. H. Joo, "Adaptive fractional fuzzy integral sliding mode control for PMSM model," *IEEE Trans. Fuzzy Syst.*, vol. 27, no. 8, pp. 1674–1686, Aug. 2019.
[21] R. Zhang, Z. Yin, N. Du, J. Liu, and X. Tong, "Robust adaptive current control of a 1.2-MW direct-drive PMSM for traction drives based on internal model control with disturbance observer," *IEEE Trans. Transp. Electrific.*, vol. 7, no. 3, pp. 1466–1481, Sep. 2021.
[22] J. Wu, J. Zhang, B. Nie, Y. Liu, and X. He, "Adaptive control of PMSM servo system for steering-by-wire system with disturbances observation," *IEEE Trans. Transp. Electrific.*, vol. 8, no. 2, pp. 2015–2028, Jun. 2022.
[23] M. Tian, B. Wang, Y. Yu, Q. Dong, and D. Xu, "Adaptive active disturbance rejection control for uncertain current ripples suppression of PMSM drives," *IEEE Trans. Ind. Electron.*, vol. 71, no. 3, pp. 2320–2331, Mar. 2024.
[24] J. Wang, Y. Liu, J. Yang, F. Wang, and J. Rodríguez, "Adaptive integral extended state observer based improved multi-step FCS-MPCC for PMSM," *IEEE Trans. Power Electron.*, vol. 38, no. 9, pp. 11260–11276, Sep. 2023.
[25] T. Orlowska-Kowalska, M. Korzonek, and G. Tarchala, "Stability improvement methods of the adaptive full-order observer for sensorless induction motor drive-comparative study," *IEEE Trans. Ind. Inform.*, vol. 15, no. 11, pp. 6114–6126, Nov. 2019.
[26] C. J. V. Filho and R. P. Vieira, "Adaptive full-order observer analysis and design for sensorless interior permanent magnet synchronous motors drives," *IEEE Trans. Ind. Electron.*, vol. 68, no. 8, pp. 6527–6536, Aug. 2021.
[27] I. D. Landau, R. Lozano, M. M'Saad, and A. Karimi, *Adaptive Control: Algorithms, Analysis and Applications*. New York, NY, USA: Springer, 2011.
[28] L. Lee and J. L. Chen, "Strictly positive real lemma and absolute stability for discrete-time descriptor systems," *IEEE Trans. Circuits Syst. I, Fundam. Theory Appl.*, vol. 50, no. 6, pp. 788–794, Jun. 2003.

Weiqiu Zhang received the B.S. degree in electrical engineering in 2020 from the Nanjing University of Aeronautics and Astronautics, Nanjing, China, where he is currently working toward the Ph.D. degree in electrical engineering.

His main research interests include the design of high-power-density inverters and advanced control strategies for high-speed and high-power electrical machines.

Zhuoran Zhang (Senior Member, IEEE) received the B.S. degree in measurement engineering in 2000 and the M.S. and Ph.D. degrees in electrical engineering in 2003 and 2009, respectively, all from the Nanjing University of Aeronautics and Astronautics (NUAA), Nanjing, China.

Since 2003, he has been a Member of the faculty with the Department of Electrical Engineering, NUAA, where he is currently a Full Professor and the Deputy Dean of College of Automation Engineering. From 2012 to 2013, he was a Visiting Professor with Wisconsin Electric Machines and Power Electronics Consortium, University of Wisconsin–Madison, Madison, WI, USA. His research interests include design and control of permanent magnet machines, hybrid excitation electric machines, and doubly salient electric machines for aircraft power, electric vehicles, and renewable energy generation.

Liyan Wen was born in Shandong, China, in 1987. She received the B.S. degree in automatic control from Shandong University, Jinan, China, in 2005, the M.S. degree in control theory and control engineering from Nanjing Normal University, Nanjing, China, in 2009, and the Ph.D. degree in control theory and control engineering from the Nanjing University of Aeronautics and Astronautics, Nanjing, in 2016.

She is currently with the College of Automation Engineering, Nanjing University of Aeronautics and Astronautics. From 2019 to 2020, she was a Visiting Assistant Professor with the Department of Electrical and Computer Engineering, University of Virginia, Charlottesville, VA, USA. Her research interests include adaptive control of multivariable systems with uncertain disturbances and actuator failures and their applications.

Weijia Jiang (Student Member, IEEE) received the B.S. degree in electrical engineering in 2022 from the Nanjing University of Aeronautics and Astronautics, Nanjing, China, where he is currently working toward the M.S. degree in electrical engineering.

His main research interests include the design of parallel hybrid excitation machine and control strategies for hybrid excitation generator.

Xiangpei Gu received the B.S. degree in electrical engineering in 2018 from the Nanjing University of Aeronautics and Astronautics, Nanjing, China, where she is currently working toward the Ph.D. degree in electrical engineering.

Her main research interests include the hybrid excitation generator design.

Yanhui Li received the B.S. degree in electrical engineering in 2021 from the Nanjing University of Aeronautics and Astronautics, Nanjing, China, where he is currently working toward the M.S. degree in electrical engineering.

His research interests include control of brushless synchronous starter/generator and electrical power generation system for more electric aircraft.